Compared prediction of the experimental failure of a thin fibrous tissue by two macroscopic damage models

Aline Bel-Brunon, Michel Coret, Karine Bruyere-Garnier, Alain Combescure

Compared prediction of the experimental failure of a thin fibrous tissue by two macroscopic damage models.

A. Bel-Brunon[a,b,c,*], M. Coret[a,b], K. Bruyère-Garnier[a,c], A. Combescure[a,b]

[a] *Université de Lyon, Lyon, F-69000, France*
[b] *INSA-Lyon, LaMCoS UMR5259, F-69621, France*
[c] *Ifsttar, UMRT9406, LBMC, F-69675, Bron, France - Université Lyon 1, F-69622, Villeurbanne, France*

Abstract

Several models for fibrous biological tissues have been proposed in the past, taking into account the fibrous microstructure through different homogenization methods. The aim of this paper is to compare theoretically and experimentally two existing homogenization methods - the Angular Integration method and the Generalized Structure Tensor method - by adapting them to a damage model for a planar fibrous tissue made of linear elastic and brittle fibers. The theoretical implementation of the homogenization methods reveals some differences once damage starts in the fibrous tissue; in particular, the anisotropy of the tissue evolves differently. The experimental aspect of this work consists in identifying the parameters of the damage model, with both homogenization methods, using inflation tests until rupture on a biological membrane. The numerical identification method is based on the simulation of the tests with the real geometry of the samples and the real boundary conditions computed by Stereo Digital Image Correlation. The identification method is applied to human liver capsule. The collagen fibers Young's modulus (19±6 MPa) as well as their ultimate longitudinal strain (33±4%) are determined; no significant difference was observed between the two methods. However, by using the experimental boundary conditions, we could observe that the damage progression is faster for the Angular Integration version of the model.

Keywords: damage model, homogenization, fibrous tissue, numerical identification, Stereo Digital Image Correlation, human liver capsule

1. Introduction

In the field of biomechanics of soft tissues, a lot of studies have been focused on the characterization of the behavior of biological tissues and organs. This is due to the numerous medical applications of a human body model, which usually remain in the physiological range of loadings. However, the potentialities of a virtual human body including information about failure of the tissues are important in several fields, including road safety and surgery. Many fatal cases caused by car crashes and reported in the literature are due to abdominal organ injuries, especially the spleen, the liver and the kidney (Tinkoff et al, 2008). Predicting the occurrence of abdominal injuries by car crash simulation would improve user safety by suggesting technical changes in the passive and active safety systems. Besides, a difficulty in abdominal surgery is to handle the organs without damaging them. Using surgical simulation to predict the overloads responsible for injuries could be useful to prevent them. For these applications, a constitutive law representing the elastic or viscoelastic behavior of a soft tissue, associated to geometrical data - e.g. external shape - and interaction data - e.g. contact behavior with neighboring organs - is not sufficient to predict injuries; a human body model also requires failure properties for these biological tissues.

Two main issues are associated with the study of soft biological tissues failure properties: advanced experimental methods are needed to guarantee the good quality of the measurements despite the softness and the living aspect of the tissues; sophisticated models are required to represent the failure mechanisms occurring in these complex and structured materials. These two features also need to be coupled so that the model complexity (number of parameters) and the experimental possi-

*Corresponding author: Lehrstuhl für Numerische Mechanik, Boltzmannstrasse 15, D-85747 Garching b. München, Germany. Email: bel@lnm.mw.tum.de .

bilities (imaging, identification) are consistent.

Investigating failure properties of soft tissues is experimentally challenging as failure is a local and unstable phenomenon that can be highly influenced by the experimental conditions. The use of full-field measurements for studying failure has been shown (Brunon et al, 2010) and is particularly adapted to soft tissues, as the boundary conditions of the experimental tests are more difficult to control and thus to repeat from one sample to the other. This is due for instance to the existence of multiple stress-free states for a soft tissue, the compression of the tissue in the clamps, the difficulty to cut samples of the same shape, etc. Also, using inflation tests to characterize biological membranes can help making the tests more repeatable as the failure does not occur at the sample edges, where some failure initiations can be created during the cutting phase. However, this loading mode is not common although it usually corresponds to more realistic loadings than uniaxial tension and guarantees a better understanding of non-linearity and possible anisotropy of the tissue (Johannknecht and Jerrams, 1999). Boyce et al. and Bischoff et al. among others have used this type of loading to characterize the cornea and artery behavior (Boyce et al, 2008; Bischoff et al, 2009). A few papers describe inflation tests on biological tissues until rupture. Mohan and Melvin determined the ultimate stress and strain of human aortic tissue using an analytic model of inflated membrane (Mohan and Melvin, 1983). Marra et al. calculated the failure strength of porcine aorta from the measurements of the global deformation and applied pressure (Marra et al, 2006). Kim et al. determined a nonlinear constitutive law and rupture criterion for the artery (Kim et al, 2011). In a previous paper (Brunon et al, 2011), we determined the hyperelastic constitutive law and ultimate strain of the liver capsule. However none of these studies consisted in the identification of a damage model.

In terms of modeling, several models for fibrous tissues are available in the literature. They consider the fibrous microstructure to drive the macroscopic behavior of the tissue. Either the distribution of the fibers and their reference state are described statistically and further identified (Lanir, 1983; Decraemer et al, 1980); or some histological evidences lead to the construction of specific representations for the microstructure, such as the structure tensor proposed in (Gasser et al, 2006). These two types of models correspond to two main homogenization methods, respectively an Angular Integration (AI) method and a Generalized Structure Tensor (GST) method. Several physical phenomena such as viscoelasticity, plasticity, growth and remodeling are also considered (Gasser et al, 2002; Gleason et al, 2005). But only a few papers address the damage of fibrous biological tissues. Some consider the damage to be solely due to fiber or fibril fracture at the microscale (Hurschler et al, 1997). Balzani et al., Calvo et al. and Rodriguez et al. all use the continuum theory to describe damage in a tissue made of a groundmatrix and bundles of fibers; they use internal macroscopic damage variables associated to either the fiber bundles solely (Balzani et al, 2006), or the fiber bundles and the groundmatrix (Calvo et al, 2006; Rodriguez et al, 2006). The evolution of the damage variables is discontinuous, *i.e.* it is based on the maximum value of an equivalent strain over the past history. In (Rodriguez et al, 2006) however, the damage in the fiber bundles is controlled by a probability density function that reflects the stochastic waviness of the fibers in their reference state; it is therefore better suited to biological soft tissues as collagen fibers are usually wavy in an unloaded biological tissue, see *e.g.* (Viidik , 1972; Orberg et al, 1982; Hill et al, 2012).

In this study, we focus on two homogenization methods proposed in the literature and investigate their differences in the range of damaging loads. The AI method proposed by (Lanir, 1983) and the GST method proposed by (Gasser et al, 2006) have been theoretically compared in (Cortes et al, 2010) for physiological ranges of loading, *i.e.* without any damage. Limits of the GST have been emphasized for fibrous distributions close to isotropy, but the differences between AI and GST methods vanish in the case of quasi-equibiaxial loading. In the present work, the experimental test case combines isotropic tissue and quasi-equibiaxial loading. The experiments are mainly devoted to provide data for the failure mechanism of this kind of tissue. But a by-product of these tests is also to produce some experimental data which allow comparing the non linear response of the two models in such a configuration.

Although several sophisticated models are available in the literature to account for various physical features - viscoelasticity *e.g.* (Limbert et al, 2004), anisotropy *e.g.* (Ateshian , 2007), fiber crimp *e.g.* (Cacho et al, 2007), etc - we chose to compare the homogenization methods using a simple model describing an isotropic fibrous membrane, made of linear elastic brittle fibers and loaded with biaxial tension. The tissue macroscopic damage is due to fiber rupture at the microscale. This is the focus of the second part of the paper. A method to identify the two versions of the obtained damage model using inflation tests and full-field measurements is then presented in the third part. The fourth part is an application of this method on human liver capsule; results are discussed in the fifth part.

2. Construction of the damage model and theoretical comparison of the homogenization methods

The proposed model consists of a damage model for the tissue that is homogenized with two homogenization methods. Some simplifying assumptions (negligible reorientation of the fibers, linear elastic behavior of the fibers or the tissue) of this academic model help making the framework as clear as possible to focus on the two main points that are the comparison of the homogenization methods and the identification method.

2.1. General framework

This section takes up the general framework of (Gasser et al, 2006).

We consider a plane tissue consisting of a groundmatrix and fibers. We consider an additive decomposition of the Helmoltz free-energy function ψ, defined per unit reference volume, into the free energy of the groundmatrix ψ_m and the free energy of the fibers ψ_f:

$$\psi = \psi_m + \psi_f \tag{1}$$

For the sake of clarity, the matrix contribution, already assessed in (Gasser et al, 2006) is not described here. Only the fibers contribution is detailed through two homogenization methods.

2.2. Description of the two homogenization methods

Let us consider a fibrous membrane made of linear elastic brittle fibers and suppose that we know the influence of a biaxial tension loading on the fibers fracture. We can proceed to homogenize the behavior. The most commonly used homogenization methods are the ones described in (Lanir, 1983) - AI method - and (Gasser et al, 2006) - GST method. The GST method has been shown to have some limitiations (Cortes et al, 2010). It is nevertheless reasonable for a quasi-equibiaxial strain state which is the case of this study. It will be extended by adding a fiber fracture model in this paper. The same extension will be proposed for the AI model.

2.2.1. The concept of fiber density function

In order to describe the strain energy in the tissue, we need to introduce the concept of angular fiber density, denoted $\rho(\xi)$. This function defines the fraction of fibers whose orientation belongs to the interval $[\xi, \xi + d\xi]$. Before damage, this function is considered to be normalized, *i.e.*:

$$\frac{1}{\pi}\int_{-\frac{\pi}{2}}^{\frac{\pi}{2}} \rho(\xi)\,\mathrm{d}\xi = \frac{1}{\pi}\int_{A_0} \rho(\xi)\,\mathrm{d}\xi = 1 \tag{2}$$

In the case of a homogeneous distribution, *i.e.* $\rho(\xi) = constant$, one has $\rho(\xi) = 1\ \forall \xi \in A_0 = [-\pi/2, \pi/2]$. Once damage starts, the density is a function of the damage state $\mathbf{D}$. In the present work, $\mathbf{D}$ defines the range of angles of the undamaged fibers *i.e.* where $\rho(\xi)$ is not null.

2.2.2. The Angular Integration (AI) homogenization method

In this method, the free energy of the fibrous part of the tissue is assumed to be the integral of the contribution of the strained, but undamaged, fibers. A fiber subjected to a Green-Lagrange strain field $\mathbf{E}$ is strained only along its longitudinal axis $\mathbf{n}(\xi)$ and its strain energy is $\phi_f = \phi_f(\varepsilon_f)$ *i.e.* $\phi_f(\xi, \mathbf{E})$, whose expression depends on the constitutive equation of the fiber. $\mathbf{n}$ is the unit vector associated to the initial orientation of the fiber. As described in the next section, we neglect the change of orientation between the fibers and the local reference frame during loading. Hence the vector $\mathbf{n}$ which represents the direction of each fiber with respect to the continuous material frame does not change during loading. Therefore, on the tissue's scale, the free energy ψ_f^{AI} of the fibers is:

$$\psi_f^{AI}(\mathbf{E}, \mathbf{D}) = \frac{1}{\pi}\int_{A_0} \rho(\xi, \mathbf{D})\phi_f(\xi, \mathbf{E})\,\mathrm{d}\xi \tag{3}$$

The expression of the second Piola-Kirchhoff stress tensor (PK2) is:

$$\mathbf{S}_f^{AI} = \frac{\partial \psi_f^{AI}(\mathbf{E}, \mathbf{D})}{\partial \mathbf{E}} = \frac{1}{\pi}\int_{A_0} \rho(\xi, \mathbf{D})\frac{\partial \phi_f(\xi, \mathbf{E})}{\partial \mathbf{E}}\,\mathrm{d}\xi \tag{4}$$

Now let us consider the simplified case where the fibers behave linearly before damage. This assumption is strong as we know that the behavior of a collagen fiber cannot be considered linear above 10% of strain (Svensson et al, 2010). The expression of stress tensor PK2 is then:

$$\mathbf{S}_f^{AI} = \frac{E}{\pi}\int_{A_0} \rho\,(\xi, \mathbf{D})\,(\mathbf{M} : \mathbf{E})\,\mathbf{M}\,\mathrm{d}\xi \tag{5}$$

where E is the Young's modulus of the fiber's material and $\mathbf{M} = \mathbf{n}(\xi) \otimes \mathbf{n}(\xi)$ the orientation tensor.

The Cauchy stress tensor is obtained using the following expression:

$$\mathbf{T} = J^{-1}\mathbf{F}.\mathbf{S}.\mathbf{F}^T \tag{6}$$

where $\mathbf{F}$ is the deformation gradient and $J = det(\mathbf{F})$. Thus:

$$\mathbf{T}_f^{AI} = J^{-1}\mathbf{F}.\mathbf{S}_f^{AI}.\mathbf{F}^T = \frac{2E}{J\pi}\mathbf{F}.\int_{A_0} \rho\left(\xi, \mathbf{D}\right)\left(\mathbf{M} : \mathbf{E}\right)\mathbf{M}\mathrm{d}\xi.\mathbf{F}^T \tag{7}$$

2.2.3. The Generalized Structure Tensor (GST) homogenization method

The GST method is derived from in (Gasser et al, 2006), among others. We introduce a generalized second-order structure tensor $\mathbf{H}$ defined by Eq.8. This tensor is used as a macroscopic projector of the strain tensor onto the structure of the undamaged fibers.

$$\mathbf{H} = \frac{1}{\pi}\int_{A_0} \rho(\xi, \mathbf{D})\mathbf{n}(\xi) \otimes \mathbf{n}(\xi)\mathrm{d}\xi \tag{8}$$

Thus, the constitutive law is applied to the tissue rather than to its constituent fibers, taking the scalar $E_h = \mathbf{H} : \mathbf{E}$ as the strain value to express the macroscopic strain energy ψ_f^{GST} . In the linear case we get:

$$\psi_f^{GST} = \frac{1}{2}E\ E_h^2 = \frac{1}{2}E\left(\mathbf{H} : \mathbf{E}\right)^2 \tag{9}$$

From that expression, we deduce the PK2 tensor corresponding to the GST model and the Cauchy stress:

$$\mathbf{S}_f^{GST} = \frac{\partial \psi_f^{GST}}{\partial \mathbf{E}} = E\left(\mathbf{H} : \mathbf{E}\right)\mathbf{H} \tag{10}$$

$$\mathbf{T}_f^{GST} = J^{-1}\mathbf{F}.\mathbf{S}_f^{GST}.\mathbf{F}^T = \frac{E}{J}\left(\mathbf{H} : \mathbf{E}\right)\mathbf{F}.\mathbf{H}.\mathbf{F}^T \tag{11}$$

2.3. A simple model for the fibers fracture

In this section, we propose a simple model to describe the evolution of the macroscopic damage denoted $\mathbf{D}$ of a planar fibrous tissue subjected to biaxial tension loading, which is assumed to be the result of fiber breakage on the microscale. This section has two objectives:

- first, to build a damage evolution law to carry out a calculation on the macroscale taking into account the anisotropic nature of the damage due to the microstructure;
- second, to compare the extension to fracture of the two homogenization methods presented in the previous section.

The underlying assumptions of this section are the following:

- the fibers are rectilinear (no initial crimp), linear elastic and brittle;
- prior to damage, the angular distribution function of the fibers is known, continuous and strictly positive;
- the phenomenon of fiber reorientation during loading is neglected;
- the *principal* directions of the biaxial strain loading do not change.

The assumption that the distribution is strictly positive helps simplifying the framework as it leads to a simple expression of the damage angles without extra condition of existence of fibers in a specific direction. The third assumption relies on the conclusions of Sacks and Gloeckner and Liao et al. which observed that the closer the loading to equibiaxiality, the lesser the reorientation of the fibers (Sacks and Gloeckner, 1999; Liao et al, 2005). Therefore, in the present study which focuses on biaxial loading close to equibiaxiality, we shall ignore fiber reorientation. This assumption helps simplifying the framework of the model. Let us quote however that the description of the damage variables evolution that is given in the paper does not require this assumption. This model is academic and is designed to produce clear conclusions when we compare the two homogenization methods proposed in the previous section. It can be extended using a two scale approach to describe more realistic situations as uncrimping, damage fibers, non isotropic fiber orientations; if they are based on statistical distributions of properties - *e.g.* in (Cacho et al, 2007) for uncrimping - the price to pay to these extensions is a larger number of internal variables to describe the small scale state and therefore, an increased computational cost and a decreased identifiability of the model.

2.3.1. Parameterization of the problem

Let us consider a planar fibrous tissue. In the material plane ($\mathbf{X_m}$,$\mathbf{Y_m}$), the direction of a fiber is characterized by the angle $\xi \in [-\pi/2, \pi/2]$ and its initial direction vector $\mathbf{n}$ defined by:

$$\mathbf{n} = \cos\xi\ \mathbf{X_m} + \sin\xi\ \mathbf{Y_m} \tag{12}$$

The tissue is subjected to a biaxial strain characterized by the macroscopic Green-Lagrange strain tensor $\mathbf{E}$ described in Cartesian coordinates by:

$$\mathbf{E} = \varepsilon_r k\,(\cos\varphi\ \mathbf{X_m} \otimes \mathbf{X_m} + \sin\varphi\ \mathbf{Y_m} \otimes \mathbf{Y_m}) \tag{13}$$

$$= E_1 \mathbf{X_m} \otimes \mathbf{X_m} + E_2 \mathbf{Y_m} \otimes \mathbf{Y_m} \tag{14}$$

where ε_r is the ultimate longitudinal strain of the fibers and φ is the loading angle. From here on, we will assume that $\varphi \in [0, \pi/2]$ and $k \geq 0$, which implies strict biaxial tension, *i.e.* no compression and possibly different amplitude in both tension directions.

The fibers constituting the tissue are uniaxial elements which can withstand only solicitations along their axis. We define the longitudinal strain ε_f of a fiber oriented along an angle ξ by:

$$\varepsilon_f = \mathbf{n}(\xi).\mathbf{E}\ \mathbf{n}(\xi) = k\varepsilon_r \left(\cos\varphi.\cos^2\xi + \sin\varphi\sin^2\xi\right) \tag{15}$$

This corresponds to the Green strain. We can observe that for $\varphi = \frac{\pi}{4}$ all the fibers are loaded equally; then, their longitudinal strain is $\varepsilon_f = \frac{k\varepsilon_r}{\sqrt{2}}$. Also, differentiating ε_f with respect to ξ shows that the most highly loaded fibers are oriented along the principal directions of the strain tensor, that is $\xi = 0$ or $\xi = \frac{\pi}{2}$, see details in (Bel-Brunon et al, 2012).

2.3.2. Initial elasticity range

The elasticity range $\mathcal{D}$ of a fiber is defined in the strain space by:

$$\mathcal{D} = \{\varepsilon_f \mid \varepsilon_f - \varepsilon_r < 0\} \tag{16}$$

The corresponding elasticity range of the tissue, denoted $\mathcal{S}$ is simply:

$$\mathcal{S} = \{\mathbf{E} \mid \forall \xi, \mathbf{n}(\xi).\mathbf{E}.\mathbf{n}(\xi) - \varepsilon_r < 0\} \tag{17}$$

The shape of $\mathcal{S}$ corresponds to the resolution of the equation $\varepsilon_f - \varepsilon_r < 0$ and is simply described by:

$$\begin{cases} k < \dfrac{1}{cos\varphi} & \forall\ \varphi \in \left[0, \frac{\pi}{4}\right] \\ k < \dfrac{1}{sin\varphi} & \forall\ \varphi \in \left[\frac{\pi}{4}, \frac{\pi}{2}\right] \end{cases} \tag{18}$$

At the boundary of $\mathcal{S}$, at least one fiber breaks as the non-rupture criterion is not respected anymore (Eq.16). The first fiber to break is always the one oriented along $\xi = 0$ if $\varphi \leq \frac{\pi}{4}$ or the one oriented along $\xi = \frac{\pi}{2}$ if $\varphi \geq \frac{\pi}{4}$. The next section describes the damage process of the fibrous tissue.

2.3.3. Evolution of the damage $\mathbf{D}$

In this paper we only mention the case of a proportional loading (*i.e.* with φ constant) for the sake of simplicity. More details on all cases can be found in (Bel-Brunon et al, 2012). Let us assume that the tissue is subjected to a proportional strain loading so as to reach a point defined by (k,φ) out of the boundaries defined by Eq.18.

The damaged state at the microscale is then defined by two subsets: the subset of healthy fibers and the subset of broken ones. These sets are defined by two angles ξ_1 and ξ_2. The vector of the two damage variables ξ_1 and ξ_2 is denoted $\mathbf{D}$ which characterizes the damage state of the tissue. These angles are obtained by the solution of inequality $\varepsilon_f(\xi) - \varepsilon_r > 0$. A proportional loading with an intensity k greater than the bounds defined in Eq.18 leads to the fracture of the fibers as follows:

$$\varphi \in \left[0, \frac{\pi}{4}\right] : \begin{cases} \text{all fibers are broken } \forall\ \xi \in [-\xi_1, \xi_1] \\ \xi_1 = \arccos\sqrt{\dfrac{1 - k\,sin\varphi}{k\,(cos\varphi - sin\varphi)}} \end{cases} \tag{19}$$

$$\varphi = \frac{\pi}{4} : \text{all fibers break simultaneously at } k = \sqrt{2}\ \text{(Eq.15)} \tag{20}$$

$$\varphi \in \left[\frac{\pi}{4}, \frac{\pi}{2}\right] : \begin{cases} \text{all fibers are broken } \forall\ \xi \in \left[-\frac{\pi}{2}, -\xi_2\right] \cup \left[\xi_2, \frac{\pi}{2}\right] \\ \xi_2 = \arccos\sqrt{\dfrac{1 - k\,sin\varphi}{k\,(cos\varphi - sin\varphi)}} \end{cases} \tag{21}$$

as detailed in (Bel-Brunon et al, 2012).

2.4. Comparison of the homogenization methods

This section compares the properties of the two homogenization methods when applied to the damage model described in the previous section. The test case

presented here corresponds to biaxial tension with a greater amplitude in the 11 direction than in the 22 direction (Fig.1); all the following plots of this section correspond to this particular loading case which leads to a slower increase of damage than equibiaxial loading and therefore, helps understanding the damage process.

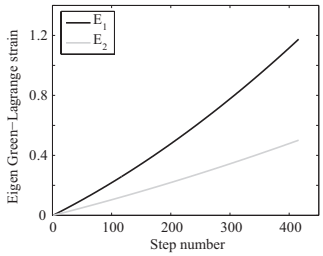

Figure 1: Components of the Green-Lagrange strain tensor of the test case.

2.4.1. *Macroscopic structure tensor properties*

An example of the evolution of the diagonal components of **H** for a loading up to rupture and for a uniform angular distribution of the fibers prior to damage, is given in Fig.2. When these two components are null, all the fibers are broken and only the groundmatrix carries the load. It can also be observed that $H_{12} = H_{21} = 0$ because the function $cos * sin$ is odd.

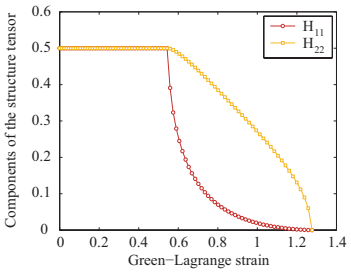

Figure 2: Evolution of the components of the structure tensor for an increasing strain amplitude.

2.4.2. *Influence of the homogenization method on the stress-strain curves*

A plot of the fibers contribution to the strain energy for each homogenization method (Fig.3) shows that under the current assumptions of uniform angular distribution prior to damage and brittle linear fibers, the two models behave differently only when fibers start to break. This difference can be observed by expanding the expressions of these energies (Eq.22,23). Let us denote X the term $\left(E_1 \cos^2\xi + E_2 \sin^2\xi\right)$. The AI fiber energy is the integral of X^2 whereas the GST one is the square of the integral of X. Indeed, we can observe that with ξ_1 and ξ_2 constant (especially prior to damage), the ratio of ψ_f^{GST} to ψ_f^{AI} is constant throughout the loading and independent of the value of the elastic parameter E.

$$\psi_f^{AI} = \frac{E}{\pi}\int_{\xi_1}^{\xi_2} (\mathbf{M}(\xi) : \mathbf{E})^2 \, \mathrm{d}\xi = \frac{E}{\pi}\int_{\xi_1}^{\xi_2} \left(E_1 \cos^2\xi + E_2 \sin^2\xi\right)^2 \mathrm{d}\xi \tag{22}$$

$$\psi_f^{GST} = \frac{E}{2}(\mathbf{H} : \mathbf{E})^2 = \frac{2E}{\pi^2}\left(\int_{\xi_1}^{\xi_2} \left(E_1 \cos^2\xi + E_2 \sin^2\xi\right) \mathrm{d}\xi\right)^2 \tag{23}$$

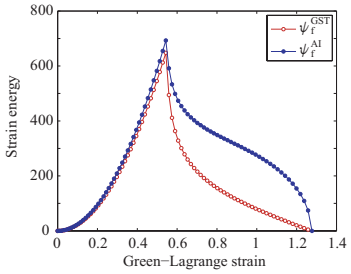

Figure 3: Comparison of the macroscopic strain energies of the fibrous tissue for the two homogenization methods with the proposed damage model for an increasing strain amplitude.

Besides, the components of tensor PK2 displayed on Fig.4(a) show that the GST model leads to the same value of the two nonzero components of $\mathbf{S}_f^{GST}$ prior to damage, whereas the tension applied to the tissue is not equibiaxial (Fig.1). Conversely, with the AI model, this unrealistic result is not obtained. This is consistent with the conclusions of both Holzapfel et al. and Cortes et al. which assess that the GST method is not adapted to isotropic distributions of fibers (Holzapfel et al, 2010; Cortes et al, 2010) if the loading is not equibiaxial. However for both models the Cauchy stress components (Fig.4,b) are consistent with the components of the strain tensor.

We can also observe a clear difference between the two homogenization methods in the concavity of the stress component in the least loaded direction. The softening part of the constitutive relation is much more anisotropic using the AI model than using the GST model. The increase of the stress observed on $T_f^{AI}(22)$

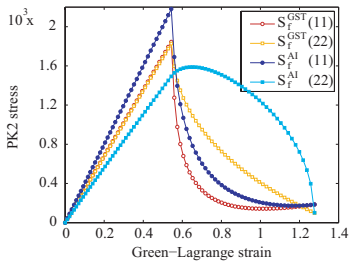

a)

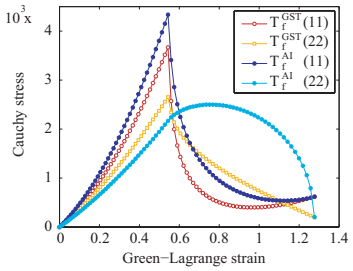

b)

Figure 4: Evolution of the tensor components of PK2 (a) and Cauchy (b) stresses as functions of the loading strain amplitude. The stress components do not revert back to 0 and start increasing after complete rupture of the fibers because of the contribution of the matrix.

just after the beginning of damage can be explained by the combination of an increasing applied strain and a relatively stable amount of load-carrying fibers in the 22 direction.

The homogenization methods have been compared on a theoretical point of view; let's now compare their behavior on an experimental case.

3. Method to determine the model parameters using inflation test

The identification method is based on the comparison of the simulated and experimental displacement fields of an inflated membrane. This section aims at describing the main steps of this procedure.

3.1. Simulation of the experimental test

The objective is to simulate the test as close as possible to the real experimental conditions, by reproducing as well as possible the geometry and boundary conditions of the sample. To do so, considering global measurement (pressure and deflection of the pole) and ideal boundary conditions (corresponding to an axisymetric configuration) is not satisfactory as they do not take

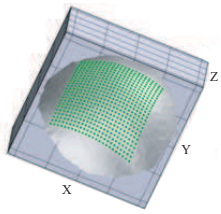

Figure 5: Nodes of the grid where the experimental displacement is caught. The simulation mesh is also defined on these nodes.

into account the possible experimental defects. Full-field measurements allow a more accurate description of the actual loading. In this paper, the field measurement was conducted using Stereo Digital Image Correlation (SDIC) via VIC3D software (Sutton et al., 2009).

A zone of interest (ZOI) was defined on the membrane surface (Fig.5, grey surface). Its shape was circular to fit the whole sample surface. We then defined a rectangular grid on the reference image of the sample. The rectangular shape was chosen to ease the meshing step and to exclude the areas close to the clamp. The SDIC computed the displacements of all the pixels of the ZOI and therefore of the nodes of the grid. The 3D geometry of the grid, computed by the SDIC, was used as the unloaded configuration of the simulation. The test was simulated with Abaqus software using *M3D4* membrane quadrangular elements. The boundary conditions of the simulation were the 3D displacement of the nodes of the grid border as well as the experimental pressure, for each correlation step. As the correlation steps may not be equally spaced and as many as the simulation steps, a linear interpolation was conducted by Abaqus between each correlation step to get the proper displacement and pressure values for each simulation steps. The output of the simulation was the 3D displacement of all the nodes inside the grid, to be compared with the experimental displacement.

3.2. Determination of the constitutive parameters

The identification consisted in minimizing the gap between the experimental and simulated vertical positions of the grid nodes of the membrane. There are several ways to measure the distance between two 3D surfaces; we chose the vertical distance which is easily measured (vertical projection) and is the most significant measure of the error for this application. The vertical position of the N nodes i at each simulation step j, stored in $\mathbf{z}^{(j)}$, was used to determine the error e between experimental and numerical position of the membrane:

$$e = \sum_{j=1}^{P} \sum_{i=1}^{N} \frac{\delta_i^{(j)}}{z_{pi}^{(j)}} \quad (24)$$

$$\delta_i^{(j)} = |z_i^{(j)} - z_{pi}^{(j)}| \quad (25)$$

with P the number of steps in Abaqus, N the number of nodes and $\delta_i^{(j)}$ the vertical gap between the experimental and numerical positions of node i at step j. One issue here was that, as mentioned above, the correlation and simulation steps did not match. The measure of the gap between the simulated and experimental positions of a node was therefore not straightforward. We chose to vertically project the simulated position on the segment linking the previous and following experimental positions. $\delta_i^{(j)}$ was the gap between the simulated position $z_i^{(j)}$ and its projection on the experimental curve $z_{pi}^{(j)}$ (Fig.6). One may pay attention to the quantity of correlation steps: the linear interpolation was satisfactory as long as the correlation steps were frequent in the non-linear areas (beginning of the curve).

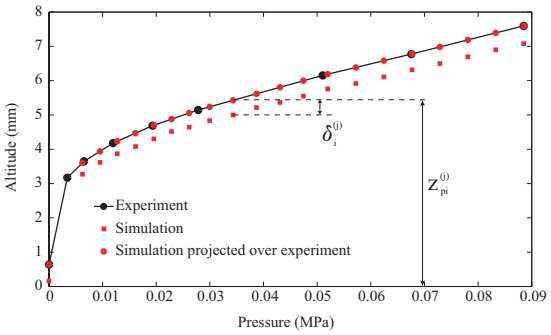

Figure 6: Measurement of the error in the vertical displacement used for the identification procedure.

The algorithm of Levenberg-Marquardt (Levenberg, 1944; Marquardt, 1963) was chosen to ensure a good convergence of the minimization of the error and implemented in Matlab. The Matlab routine wrote the successively required Abaqus input files, launched the Abaqus simulations using the *command* function, and compiled and ran the Fortran post-treatment files to get the node displacements. The obtained simulated displacements were read to build the Jacobian matrix and to further update the material parameters and the regularization factor. Several initial guesses were tested to ensure that the identified parameter corresponded to a global minimum.

In the case of the present damage model, the three parameters to identify were the fibers and the groundmatrix Young's moduli, as well as the fibers ultimate strain. As the contributions of both the matrix and the fibers are independent, the solution of the identification of the Young's moduli is not unique. An additional statement was necessary; in the present paper, we assumed that the matrix had a very small influence. Its modulus has been chosen to be about one thousand times smaller than the fibers modulus. Preliminary studies within this work led to choose a value of 0.01 MPa.

The determination of the fibers ultimate longitudinal strain was conducted using the ultimate pressure and deformation state of the material. As mentioned before, the matrix was much softer than the fibers. Therefore, a classical Finite Element simulation, without any improved tool to compute failure (such as X-FEM), lead to a divergent result once the fibers break. SDIC was conducted until the last image before the sample rupture, corresponding to a pressure p_{last}. We assumed then that the pressure increase Δp between two images was constant at this stage, so that the ultimate pressure was known ($p_{ult} = p_{last} + \Delta p$). The image and pressure acquisition frequency of 50 Hz is fast enough to ensure a small pressure increase between two images and therefore, a good estimation of the rupture pressure. The fiber ultimate strain corresponded to a divergent computation for this specific pressure.

4. Application to human liver capsule

The damage model and identification procedure presented in the previous sections were applied to human liver capsule. This tissue can indeed be considered as isotropic as confocal microscopy on the collagen fibers of the capsule did not reveal any preferred direction (Brunon et al, 2011). The experimental protocol has been presented in a previous paper (Brunon et al, 2011); the main features are recalled here.

4.1. Experimental set-up

Inflation tests were conducted on 15 samples of human liver capsule, all from the same liver. After being covered with a fine random pattern, the circular samples were fixed between two silicone flat seals (ϕ_{int} = 25 mm, ϕ_{ext} = 30 mm) on a PMMA plate (Fig.7). The circular shape of the samples was chosen so that the inflation test corresponded to rather equibiaxial tension. The capsule being translucent allowed a throughout lighting which prevented possible light reflections on the camera sensors and ensured a good SDIC. The capsule was inflated with air at a strain rate of approximately 10^{-2} s^{-1} before rupture. The deformation of the capsule was recorded by two digital DALSA cameras associated to two 35

mm macro-lenses to have the appropriate size (20 × 20 mm^2) and depth of field (around 10 mm). The pressure was recorded using a 3-bar ENTRAN EPX-N1 pressure sensor (accuracy ± 1%).

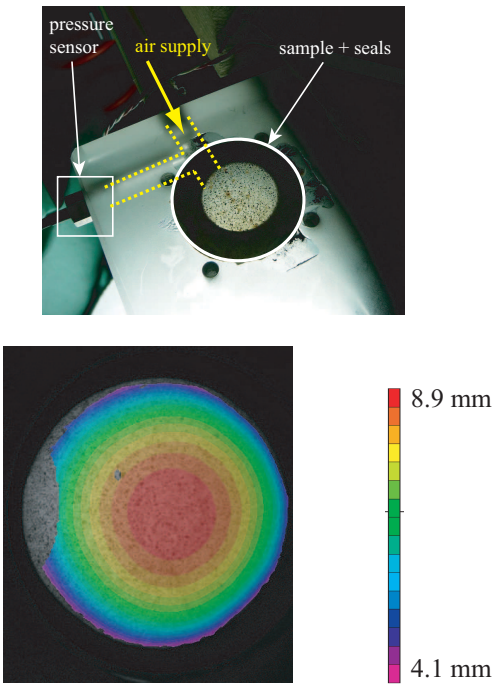

Figure 7: Top: experimental device: view of the dedicated system to load the sample (without the clamp and screws) when illuminated. Bottom: Example of the vertical displacement field (in mm) computed by stereocorrelation on the inflated capsule.

4.2. Simulation of the test

The method to simulate the test is described in Sec.3.1 but some details specific to this application are given here.

For the simulation, the thickness of the capsule was assumed homogeneous throughout the liver. Its value was set to 0.1 mm, corresponding to a typical mean value of measured thicknesses in previous studies (Snedeker et al, 2005; Hollenstein et al, 2006; Brunon et al, 2010). The number of elements was fixed by the grid size - 0.5×0.5 mm^2 - of the SDIC. The number of elements depended on the sample and was around 500.

The reference - unloaded - state of the capsule was defined after computing the position of the capsule by SDIC. We set the reference state to be the first state (image) with a constant curvature sign. This means that there was no more wrinkling and that the displacements further computed relative to this reference state would be consistent. The capsule was therefore slightly inflated at this reference state; the initial pressure was measured around 0.002 MPa, corresponding to less than 4% of the maximal measured pressure. The main difficulty as we will see in the next section is the control of the clamping conditions. In order to have a good modeling of the real boundary conditions, the SDIC-computed displacements have been used to set the boundary conditions of the model.

The simulation was conducted using an explicit procedure. This resulted in vibrations of the capsule if the simulation speed was the real one. Therefore the simulated test was five times slower than the experimental test; this ensured a good representation of the beginning of the deflection curve and a good convergence of the identification algorithm.

To ease the convergence of the identification, the optimization procedure was conducted in two steps: we first minimized the error on the pole of the sphere vertical position ; this gave a first estimation of the parameters. Then we adjusted these previously determined parameters using the error on all the nodes of the capsule. This method revealed that the position of the pole was a rich enough information to identify the parameters of the damage law, as the optimization of the parameters during the second phase lead to less than 5% of variation of the identified parameters provided the experimental boundary conditions are correctly modeled.

4.3. Results

As mentioned in (Brunon et al, 2011), the experimental strain field did not correspond to an ideal axisymetric inflation test. Due to their softness, the silicone seals wrinkled while being compressed and made the clamping not flat. Also, a few samples experienced slippage. This shows the need for full-field measurements to ensure the correspondence between the experimental test and the simulated one.

Fig.8 shows the result of the identification of the fibers Young's modulus. The matrix modulus was chosen to be 0.01 MPa as preliminary studies showed that the fibers modulus would be in the order of 10 MPa. This lead to a value of 19 ± 6 MPa for the fibers elasticity (Tab.1). This value corresponds to an error between the experimental and simulated displacements of 4% when averaged over all the nodes and steps. It is obvious here that the linear assumption is not sufficient as it is too stiff at the beginning and not enough for larger strains. No significant difference was detected between the AI and the GST versions of the model; this is due to the assumption of linear behavior for the fiber - or for

Sample nb	E (MPa)	ε_r^{AI}(-)	ε_r^{GST} (-)
1	10.0	0.435	0.345
2	20.0	0.290	0.275
3	19.6	0.305	0.275
6	30.5	-	-
7	24.0	0.390	0.345
8	19.8	-	-
9	20.0	0.355	0.340
10	11.3	0.290	0.275
11	25.3	-	-
12	14.9	0.345	0.335
13	25.4	0.315	0.300
14	14.0	0.365	0.360
15	12.1	-	-

Table 1: Identified values of the fibers Young modulus and determined values of their ultimate strain, for both *AI* and *GST* homogenization method. Cells exhibiting "-" correspond to samples that experienced slippage and did not break. Only the values of Young's modulus obtained with the *AI* method are displayed as they were the same as the ones obtained with the *GST* method.

the whole fibrous tissue - which makes the two models equivalent without any damage.

For the identification of the ultimate strain ϵ_r, the ultimate pressure was set to 105% of the pressure corresponding to the last image before rupture, as explained in Sec.3.2. A mean value of 33 ± 4% is obtained. The two versions of the model give approximately the same results in terms of ultimate strain of the fiber.

Fig.9 shows the failure surface obtained with both model. With ideal boundary conditions, the capsule sample being circular would lead to an equal loading on all the fibers and a brutal rupture of all the fibers at the same step. Using the experimental boundary conditions leads to a non-equibiaxial loading and a more localized rupture, especially with the *GST* version model. We can see the damage and the strain concentration in several elements (light to dark blue). The *AI* version of the model leads to a faster increase of damage in all the elements: the loading is indeed much more biaxial with this version once the damage occurs than with the *GST* version, as we can see on the Fig.4; the stress in the less loaded direction is still quite high while it drops really fast in the *GST* version.

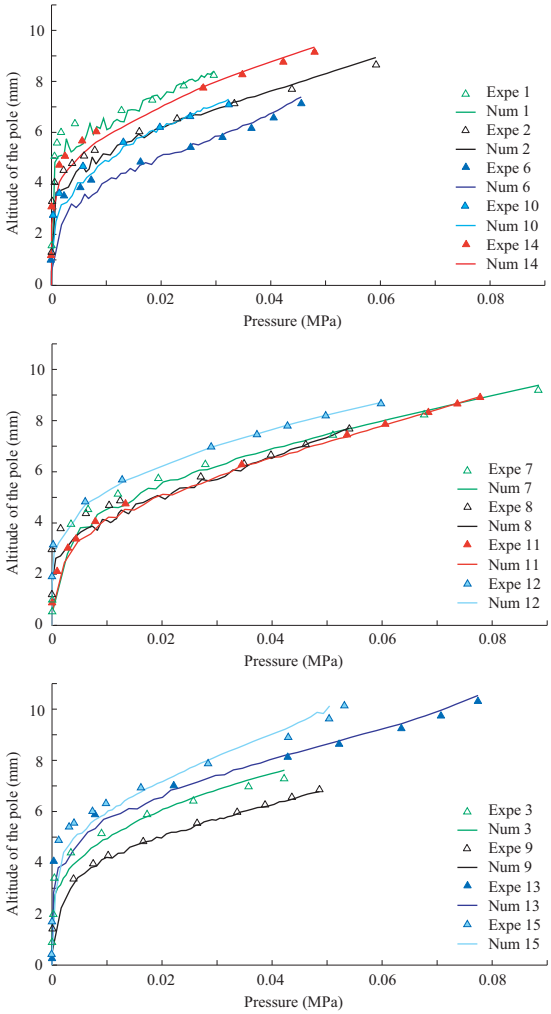

Figure 8: Identification of the *GST* version of the damage model for human hepatic capsule. *Expe* and *Num* are experimental data and simulated data respectively.

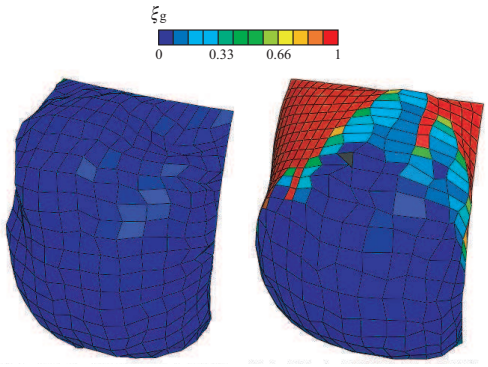

Figure 9: Comparison of the failure surface obtained with both homogenization methods (left:AI, right:GST). $\xi_g = \frac{2}{\pi}(\xi_2 - \xi_1)$ so $\xi_g = 1$ (red) with no damage and decreases to 0 (blue) when damage increases.

5. Discussion

This paper presents the comparison between two homogenization methods on the theoretical and experimental point of views. It gives a first estimation of the material properties of the human liver capsule through a realistic loading. Biaxial tension is close to what the liver surface experiences on one region if it is compressed on the other side (which is typical of crash loading situations). However more samples from more livers should be tested to give an actual value for the identified parameters.

The damage model described in this paper is adapted to the human liver capsule as its fiber angular distribution is homogeneous (Brunon et al, 2011). It allows a satisfactory description of this tissue within a small number of parameters, which makes the identification procedure rather robust. The assumption of linear elasticity for the elastic part is however not correct even if the strain only reaches 30%; as seen in (Brunon et al, 2011), a non-linear law could represent more accurately the increase of stiffness as the strain increases. Of course more sophisticated damage models available in the literature would better describe some physical features of the capsule, such as its non-linearity, its viscoelasticity (not mentioned in this paper but existing as in most of the biological tissues), the fiber crimp or the damage nature of the fibers themselves. However, such features were not in the scope of this study which first, was focused on the homogenization methods and second, aimed at describing the tissue with very few parameters to allow a robust identification. The construction of the model in its two versions showed that the homogenization methods differ significantly once damage starts. Also it revealed a non-physical behavior for the second Piola-Kirchhoff tensor when the GST method is applied to an isotropic planar tissue loaded with non-equibiaxial tension.

The identified parameters (fibers Young's modulus and ultimate longitudinal strain) are a preliminary estimation as all the samples come from the same liver. The groundmatrix elasticity modulus, which is a parameter of the complete model, cannot be identified using this protocol for two reasons: the parallel contribution of both the fibers and the groundmatrix leads to a non-unique solution for the identification of their Young's moduli; the groundmatrix contribution to the overall energy and stress is very low in a connective tissue, so that the experimental noise prevents a robust identification of its elasticity. Therefore the matrix elasticity modulus was set up to an arbitrary low value. Comparing the fibers Young's modulus obtained here to values from the literature would require better knowledge on the tissue microstructure. The capsule is mainly made of collagen fibers of type I and III. The value of 19 MPa is rather low compared to those from the literature that range for collagen of type I from 0.4 to 3 GPa (Fung, 1993; Sasaki and Odajima, 1996; Carlisle et al, 2010). Only one paper has comparable values (Lopez-Garcia et al, 2010). A quantification of the microstructure would be necessary to explain this discrepancy; previous studies showed indeed the strong influence of structure over stiffness of the collagen (Gautieri et al, 2011).

On the other hand, the ultimate strain determined using this damage model can be compared to the literature as it does not depend on the quantity of fibers in each direction. The value of 33 ± 4% is in the range of the the one assessed in (Carlisle et al, 2010).

The main feature of the identification method is the simulation of the test using experimental boundary conditions. One of the main issues when testing soft tissues is to ensure the repeatability of the boundary conditions from one sample to the other. The need for special clamping technics, that do not damage the sample and prevent any sliding implies that the boundary conditions are not perfectly controlled, especially with such a thin tissue. Using full-field measurement with high quality images allows determining the actual strain field on the sample rather accurately. In our case, several samples experienced slippage or wrinkled stress free states but these experimental characteristics are caught by the SDIC and included in the simulation. Once automatized, the identification procedure can therefore take into account the variability of the experimental conditions, to improve the material parameters determination. Simulating the tests using the experimental boundary

conditions allows the comparison between the two versions of the damage model. In the inflation test case, the tissue is loaded with pressure; this emphasizes the difference in damage progression between the two homogenization methods.

The main issue of the experimental protocol is that the membrane failure occurs rather rapidly, which does not allow the control of the damage evolution. This is due to two main reasons. First, the capsule was inflated with air, which is compressible. When the failure started, the compressed air was suddenly released and made the failure grow almost instantly. This could be improved by applying the load using water instead of air: as water is incompressible, the membrane displacement during inflation would be more directly controlled, especially when failure occurs. Second, the circular shape of the clamping made the load almost equibiaxial. As the membrane was initially isotropic, this lead to an equal loading of all the fibers, as shown in the model description. An elliptic instead of circular clamping could allow a slower increase of the damage into the tissue and therefore, it could be caught by the SDIC system.

The identification method presented here can be adapted to any soft tissue membrane. Existing or user-defined constitutive laws can be accurately identified as the experimental conditions are correctly simulated. For this particular application, future work would consist in implementing non-linear potential for the fibers in the damage model and modifying the experimental set-up to ensure a better control of the failure (shape of the clamp, loading with an incompressible fluid). An interesting prospect would also be to identify both contributions of the fibers and the groundmatrix; this could be achieved by treating the tissue with collagenase to destroy the collagen fibers and characterize the groundmatrix alone, as done in (Rausch et al, 2012). More advanced identification methods could also be adapted to this model such as the virtual field method - already used for a similar protocol in (Kim et al, 2011) - or the Integrated Mechanical Image Correlation (I-MIC, see (Réthoré, 2010)). Such methods improve the noise sensitivity of the optimization procedure.

Acknowledgement 1. *The authors would like to thank the Region Rhone-Alpes for its financial support as well as Adrien Charmetant for his technical support .*

References

Ateshian GA (2007) Anisotropy of fibrous tissues in relation to the distribution of tensed and buckled fibers. Journal of biomechanical engineering 129:240–249

Balzani D, Schröder J, Gross D (2006) Simulation of discontinuous damage incorporating residual stresses in circumferentially overstretched atherosclerotic arteries. Acta Biomaterialia 2(6):609–618

Bel-Brunon A, Coret M, Bruyère-Garnier K, Combescure A (2012) Comparaison of two homogenization methods using a damage model for a fibrous membrane, based on the fibers' fracture process at the microscale. European Journal of Mechanics - A/Solids 39:1–10

Bischoff J, Drexler E, Slifka A, McCowan C (2009) Quantifying nonlinear anisotropic elastic material properties of biological tissue by use of membrane inflation. Computer Methods in Biomechanics and Biomedical Engineering 12(3):353–369

Boyce B, Grazier J, Jones R, Nguyen T (2008) Full-field deformation of bovine cornea under constrained inflation conditions. Biomaterials 29(28):3896–3904

Brunon A, Bruyère-Garnier K, Coret M (2010) Mechanical characterization of liver capsule through uniaxial quasi-static tensile tests until failure. Journal of Biomechanics 43(11):2221–2227

Brunon A, Bruyère-Garnier K, Coret M (2011) Characterization of the nonlinear behaviour and the failure of human liver capsule through inflation tests. Journal of the Mechanical Behavior of Biomedical Materials 4(8):1572–1581

Cacho F, Elbischger PJ, Rodriguez JF, Doblare M, Holzapfel GA (2007) A constitutive model for fibrous tissues considering collagen fiber crimp. International Journal of Non-Linear Mechanics 42(2):391–402

Calvo B, Pena E, Martinez MA, Doblare M (2006) An uncoupled directional damage model for fibred biological soft tissues. Formulation and computational aspects. International Journal for Numerical Methods in Engineering 06:1–30

Carlisle C, Coulais C, Guthold M (2010) The mechanical stress-strain properties of single electrospun collagen type I nanofibers. Acta Biomaterialia 6(8):2997–3003

Cortes DH, Lake SP, Kadlowec JA, Soslowsky LJ, Elliott DM (2010) Characterizing the mechanical contribution of fiber angular distribution in connective tissue: comparison of two modeling approaches. Biomechanics and Modeling in Mechanobiology 9:651–658

Decraemer WF, Maes M, Vanhuyse VJ (1980) An elastic stress-strain relation for soft biological tissues based on a structural model. Journal of Biomechanics 13:463–468

Fung Y (1993) Biomechanics: mechanical properties of living tissues, vol 12. Springer

Gasser T, Holzapfel G (2002) Modeling the propagation of arterial dissection. European Journal of Mechanics-A/Solids 25(4):617–633

Gasser T, Ogden R, Holzapfel G (2006) Hyperelastic modelling of arterial layers with distributed collagen fibre orientations. Journal of the royal society interface 3(6):15

Gautieri A, Vesentini S, Redaelli A, Buehler M (2011) Hierarchical structure and nanomechanics of collagen microfibrils from the atomistic scale up. Nano Letters 11(2):757–766

Gleason RLJR, Humphrey D (2005) A 2D constrained mixture model for arterial adaptations to large changes in flow, pressure and axial stretch. Mathematical Medecine and Biology 22:347–396

Hill MR, Duan X, Gibson GA, Watkins S, Robertson AM (2012) A theoretical and non-destructive experimental approach for direct inclusion of measured collagen orientation and recruitment into mechanical models of the artery wall. Journal of Biomechanics 45:762–71

Hollenstein M, Nava A, Valtorta D, Snedeker J, Mazza E (2006) Mechanical Characterization of the Liver Capsule and Parenchyma. Lecture notes in computer science 4072:150–158

Holzapfel GA, Ogden RW (2010) Constitutive modelling of arteries. Proceedings of the Royal Society A: Mathematical, Physical and

Engineering Science 446(2118):1551–1597
Hurschler C, Loitz-Ramage B, Vanderby JR (1997) A structurally based stress-stretch relationship for tendon and ligament. Journal of biomechanical engineering 119:392–399
Johannknecht R, Jerrams S (1999) The need for equi-biaxial testing to determine elastomeric material properties. In: Proceedings of the First European Conference on Constitutive Models for Rubber, Vienna, Austria, 9-10 September 1999, Taylor & Francis, 73–76
Kim J, Avril S, Duprey A, Favre J (2011) Experimental characterization of rupture in human aortic aneurysms using a full-field measurement technique. Biomechanics and Modeling in Mechanobiology 11(6):841–853
Lanir Y (1983) Constitutive equations for fibrous connective tissues. Journal of Biomechanics 16:1–12
Levenberg K (1944) A method for the solution of certain problems in least squares. Quarterly of Applied Mathematics 2:164–168
Liao J, Yang L, Grashow J, Sacks M (2005). Molecular orientation of collagen in intact planar connective tissues under biaxial stretch. Acta Biomaterialia 1:45–54
Limbert G, Middleton J (2004) A transversely isotropic viscohyperelastic material:: Application to the modeling of biological soft connective tissues. International journal of solids and structures 41(15):4237–4260
Lopez-Garcia M, Beebe D, Crone W (2010) Young's modulus of collagen at slow displacement rates. Bio-Medical Materials and Engineering 20(6):361–369
Marquardt D (1963) An algorithm for least-squares estimation of nonlinear parameters. Journal of the society for Industrial and Applied Mathematics 11(2):431–441
Marra S, Kennedy F, Kinkaid J, Fillinger M (2006) Elastic and rupture properties of porcine aortic tissue measured using inflation testing. Cardiovascular Engineering 6(4):123–131
Mohan D, Melvin J (1983) Failure properties of passive human aortic tissue. ii–biaxial tension tests. Journal of Biomechanics 16(1):31–37
Orberg JW, Klein L, Hiltner A (1982) Scanning electron microscopy of collagen fibers in intestine. Connective tissue research 9(3):187–193
Rausch S, Pack O, Martin C, Uhlig S, Wall W (2012) Development of a constituent-based material model for soft biological tissue - using the example of lung parenchyma. Journal of the Mechanical Behavior of Biomedical Materials, submitted.
Réthoré J (2010) A fully integrated noise robust strategy for the identification of constitutive laws from digital images. International Journal for Numerical Methods in Engineering 84 (6):631–660
Rodríguez JF, Cacho F, Bea JA, Doblaré M (2006) A stochastic-structurally based three dimensional finite-strain damage model for fibrous soft tissue. Journal of the Mechanics and Physics of Solids 54(4):864–886
Sacks M, Gloeckner D (1999) Quantification of the fiber architecture and biaxial mechanical behavior of porcine intestinal submucosa. Journal of biomedical materials research 46(1):1–10
Sasaki N, Odajima S (1996) Elongation mechanism of collagen fibrils and force-strain relations of tendon at each level of structural hierarchy. Journal of biomechanics 29(9):1131–1136
Snedeker J, Niederer P, Schmidlin F, Farshad M, Demetropoulos C, Lee J, Yang K (2005) Strain-rate dependent material properties of the porcine and human kidney capsule. Journal of Biomechanics 38(5):1011–1021
Sutton M, Orteu J, Schreier H (2009) Image correlation for shape, motion and deformation measurements: basic concepts, theory and applications. Springer Verlag.
Svensson RB, Hassenkam T, Hansen P, Magnusson SP (2010) Viscoelastic behavior of discrete human collagen fibrils. Journal of the Mechanical Behavior of Biomedical Materials 3:112–115
Tinkoff G, Esposito T, Reed J, Kilgo P, Fildes J, Pasquale M, Meredith J (2008) American Association for the Surgery of Trauma Organ Injury Scale I: spleen, liver, and kidney, validation based on the National Trauma Data Bank. Journal of the American College of Surgeons 207(5):646–655
Viidik A (1972) Simultaneous mechanical and light microscopic studies of collagen fibers. Zeitschrift für Anatomie und Entwicklungsgeschichte 136(2):204–212